Journal of Power Sources 196 (2011) 8424–8434

Contents lists available at ScienceDirect

Journal of Power Sources

journal homepage: www.elsevier.com/locate/jpowsour

A multi-level simulation platform of natural gas internal reforming solid oxide fuel cell–gas turbine hybrid generation system – Part II. Balancing units model library and system simulation

Cheng Bao[a,b,*], Ningsheng Cai[b], Eric Croiset[b,c]

[a] Department of Thermal Science and Energy Engineering, School of Mechanical Engineering, University of Science & Technology Beijing, Beijing 100083, PR China
[b] Key laboratory for Thermal Science and Power Engineering of Ministry of Education, Tsinghua University, Beijing 100084, PR China
[c] Department of Chemical Engineering, University of Waterloo, Waterloo, Ontario N2L 3G1, Canada

ARTICLE INFO

Article history:
Received 2 March 2011
Received in revised form 10 May 2011
Accepted 12 May 2011
Available online 20 May 2011

Keywords:
Solid oxide fuel cell
Gas turbine
Multi-level modeling
Neural network
Reverse design
Part-load and dynamic

ABSTRACT

Following our integrated hierarchical modeling framework of natural gas internal reforming solid oxide fuel cell (IRSOFC), this paper firstly introduces the model libraries of main balancing units, including some state-of-the-art achievements and our specific work. Based on gPROMS programming code, flexible configuration and modular design are fully realized by specifying graphically all unit models in each level. Via comparison with the steady-state experimental data of Siemens–Westinghouse demonstration system, the in-house multi-level SOFC–gas turbine (GT) simulation platform is validated to be more accurate than the advanced power system analysis tool (APSAT). Moreover, some units of the demonstration system are designed reversely for analysis of a typically part-load transient process. The framework of distributed and dynamic modeling in most of units is significant for the development of control strategies in the future.

© 2011 Elsevier B.V. All rights reserved.

1. Introduction

As a candidate for more efficient power generation than the conventional power plants, the combined cycle by solid oxide fuel cell (SOFC) and gas turbine (GT) attracts extensive attention in the worldwide. Modeling and simulation plays an important role in the development of SOFC–GT hybrid generation technology. In general, various system configurations and numerical requirements call for modular simulation with different complexities. Recently, we have developed an in-house multi-level simulation platform for SOFC–GT hybrid generation system in the commercial environment of gPROMS [1]. The integrated hierarchical modeling framework of natural gas internal reforming SOFC has been firstly introduced in our previous work [2].

In addition to the multi-scale modeling of fuel cell and stack, models of other balancing units including the gas turbine, reformer, heat exchanger, ejector, burner, splitter, mixer, etc. are indispensable for system-level analysis. Table 1 exhibits the representative work on modeling and simulation of SOFC or molten carbonate fuel cell (MCFC) combined heat and power plant and SOFC–GT or MCFC–GT hybrid system in the worldwide institutes [1–22]. In general, the model-based analyses of high temperature fuel cell power plant can be summarized as follows:

(1) Analysis of full-load and part-load operation performance and parameter optimization based on the first and second law of thermodynamics.
(2) The safe or healthy operation range of parameters including the SOFC temperature, turbine inlet temperature (TIT), pre-reforming temperature, surge margin of the compressor, steam–carbon ratio, and pressure difference between the anode and cathode side in case of gas recycling, etc.
(3) The necessity of introducing controllers and various control strategies, for example, the fixed gas flow rate or fixed gas utilization, fixed or variable turbine speed, the different temperature control modes including NFCRC mode, NETL mode and cascading control, etc.
(4) Technology of networked stacks or stack stage which focuses on analysis of local fuel and air utilization, current and temperature distribution among the serially or parallel connected stacks. And some new configurations, such as FC-Reformer-FC concept by using an external reformer as the intercooler of the upstream stack outlet air.

* Corresponding author. Tel.: +86 10 62333682; fax: +86 10 62329145.
E-mail address: baocheng@mail.tsinghua.edu.cn (C. Bao).

0378-7753/$ – see front matter © 2011 Elsevier B.V. All rights reserved.
doi:10.1016/j.jpowsour.2011.05.032

Nomenclature

A	Area (m^2) or pre-exponential factor in Eq. (12)
a, b, c	Fitting variables
c	Concentration ($mol\,m^{-3}$)
C	Heat capacity rate ($W\,K^{-1}$)
c_p	Mass specific heat ($J\,kg^{-1}\,K^{-1}$)
d	Diameter (m)
E	Activation energy ($J\,mol^{-1}$)
h	Mass specific enthalpy ($J\,kg^{-1}$) or convective heat transfer coefficient ($J\,m^{-2}\,s^{-1}$)
Δh	Mass specific enthalpy difference or polytropic head ($J\,kg^{-1}$)
k	Adiabatic index
K_{eq}	Equilibrium constant (bar^2 or 1)
M	Molecular weight ($kg\,mol^{-1}$)
$\dot{m}$	Mass flow rate ($kg\,s^{-1}$)
N	Turbomachinery rotational speed (rpm)
N_{cr}	Corrected speed parameter ($rpm\,K^{-0.5}$)
NTU	Number of heat transfer units
p	Pressure (Pa)
p_0	Standard atmospheric pressure (Pa)
P	Power (kW)
r	Volumetric reaction rate ($mol\,m^{-3}\,s^{-1}$) or radius (m)
R	Universal gas constant ($8.314\,J\,mol^{-1}\,K^{-1}$)
t	Time (s)
T	Temperature (K)
u	Velocity ($m\,s^{-1}$)
$\dot{V}$	Volumetric flow rate ($m^3\,s^{-1}$)
x	Molar fraction
z	Axial coordinate (m)

Greek

α	Total heat transfer area per volume of heat exchanger ($m^2\,m^{-3}$)
β	β parameter in β line model
ε	Effectiveness of heat exchanger
ε_P	Void of packed bed
η	Efficiency
κ	Heat conductivity ($W\,m^{-1}\,K^{-1}$)
μ	Dynamic viscosity (Pa s)
π	Pressure ratio
ϕ	Corrected mass flow parameter ($kg\,s^{-1}\,K^{0.5}\,bar^{-1}$)
ρ	Density ($kg\,m^{-3}$)
σ	The ratio of flow area (A_{free}) to frontal area (A_{fr}) of heat exchanger ($m^2\,m^{-2}$)

Subscripts and superscripts

0	Design point
c	Compressor or cold fluid
cat	Catalyst
g	Gas
h	Hot fluid
in	Inlet
max	Maximum
min	Minimum
out	Outlet
ref	Reference or reforming reaction
s	Isentropic process
shift	Water gas shift reaction
t	Turbine or total
w	Wall

(5) Methods to improve the flexibility of the system by adopting an external combustor and bypass valves for fast start-up and temperature control.

This paper firstly introduces the model library of main balancing units in our SOFC–GT simulation platform, which includes some achievements in the state-of-the-art literatures and our specific work. Secondly, in a gPROMS commercial environment, all unit models in different level are graphically specified and validated by the steady-state experimental data of Simense–Westinghouse demonstration system. Finally a transient operation with variable load is analyzed based on the reverse design of units.

2. Model libraries of balancing units

2.1. Turbomachinery

2.1.1. Isentropic efficiency model

The simplest and the most general method of modeling compressor and turbine (C/T) is the so-called isentropic efficiency model, that is

$$\eta_c = \frac{h_{s,c}(T_{s,c}) - h_{in}(T_{in})}{h_{out}(T_{out}) - h_{in}(T_{in})}, \quad \eta_t = \frac{h_{in}(T_{in}) - h_{out}(T_{out})}{h_{in}(T_{in}) - h_{s,t}(T_{s,t})} \tag{1}$$

where η_c and η_t are the compressor and turbine efficiency, h_{in} and h_{out} are the mass specific enthalpy of inlet and outlet gas, h_s is the mass specific enthalpy for isentropic process, T_{in} and T_{out} are the inlet and outlet gas temperatures. For ideal gas in an isentropic process, the discharge temperature, T_s is related to the pressure ratio of compressor or turbine ($\pi_c = p_{out}/p_{in}$, $\pi_t = p_{in}/p_{out}$)

$$T_{s,c} = T_{in}\pi_c^{(k-1)/k}, \quad T_{s,t} = T_{in}\pi_t^{-(k-1)/k} \tag{2}$$

where k is the ratio of specific heats or adiabatic index.

For a mass flow rate $\dot{m}$, the power of compressor or turbine is the enthalpy difference between the inlet and outlet gas

$$P_c = \dot{m}_c(h_{out} - h_{in}), \quad P_t = \dot{m}_t(h_{in} - h_{out}) \tag{3}$$

2.1.2. Some state-of-the-art turbomachinery models

The Process Model Library (PML) of flow transportation in gPROMS provides a fan model of centrifugal compressor [23]. According to Fan laws, the compressor performance between the operating point and the design point (with subscript 0) is related as

$$\frac{\dot{V}}{\dot{V}_0} = \frac{N}{N_0}, \quad \frac{\Delta h}{\Delta h_0} = \left(\frac{N}{N_0}\right)^2 \tag{4}$$

where $\dot{V}$ is the volumetric flow rate, N is the compressor rotational speed, Δh is the mass specific enthalpy difference between the discharge and suction gas (or polytropic head). And the compressor efficiency is considered independent on the compressor speed.

The Jensen & Kristensen (J/K) model has been widely used in modeling of the turbocharger of internal combustion engines [24]. In J/K compressor model, the dimensionless head parameter and compressor efficiency are expressed as functions of the normalized flow rate and the inlet Mach number. In J/K turbine model, in additional to the nozzle equation, the turbine efficiency is expressed as a polynomial function of the corrected turbine speed parameter and the blade–speed ratio, which is also suitable for variable nozzle turbines.

Without physical meaning of β, β line model is a purely mathematical method. As shown in Fig. 1, β lines are a set of equally spaced parabolas or straight lines, which have a unique intersection point with each constant speed line [12,17,25]. By setting two parabolic lines at $\beta = 0$ and $\beta = 1$ (each determined by three data

Table 1
Representative work on modeling and simulation of SOFC/MCFC based system.

Institute	Country	Main research contents and achievements
National Fuel Cell Research Center (NFCRC)	U.S.A.	Advanced power systems analyses tools (APSAT), energy and exergy analyses of single-stage and two-stage SOFC-Humid Air Turbine (HAT) cycle, necessity of introducing controllers, different temperature control mode including NETL mode, NFCRC mode and cascading control [3,4]
National Energy Technology Laboratory (NETL)	U.S.A.	Reasonable air recycling in the cathode and technology of stack stage, and comparison among the thermodynamic performance of various external reforming and internal reforming hybrid configurations [5]
University of Wisconsin-Madison	U.S.A.	EES-based modeling of SOFC system for small-scale stationary application, configuration with anode and cathode gas recycling, optimal system design and comparison among three control modes [6]
The Pennsylvania State University, Park University	U.S.A.	Lumped and control-oriented modeling of MCFC power plant, decentralized controller design for the stack temperature, pressure difference, fuel utilization and steam–carbon ratio [7]
University of Genova	Italy	TRANSEO simulation tool, full-load and part-load performance of SOFC/MCFC–GT system, effects and control strategies of gas flow rates, gas recirculation ratio, turbine speed, bypass valve, etc. [8,9]
University of Perugia	Italy	Temperature control strategies using four-way valve in an atmospheric MCFC–GT power plant [10]
Juelich Research Center	Germany	Modeling of combined SOFC CHP plant based on Pro/II, analysis of various parameters including internal reforming, air inlet temperature, fuel utilization, and gas recycling in the anode and the cathode [11]
Norwegian University of Science and Technology	Norway	gPROMS-based toolbox for SOFC–GT power plant, system design, steady-state part-load performance, transient operation and decentralized controller [12]
Lund University	Sweden	AspenPlus-based analysis of full-load operation of SOFC–GT system, networked SOFC stacks [13,14]
Delft University of Technology	Netherlands	MCFC power plant with gas recirculation and waste heat utilization in the form of an expander and steam production cycle, influence of operating temperature on system performance [15]
University of Waterloo	Canada	AspenPlus-based modeling and simulation of Siemens Westinghouse SOFC–GT hybrid system [16]
Nanyang Technological University	Singapore	Component matching in IRSOFC–GT power plant, performance analysis of heat and power cogeneration, configuration with an afterburner between SOFC stack and GT [17]
University of Tokyo, Nippon Telegraph and Telephone Corp.	Japan	Conceptual design of a 30 kW-scale SOFC–MGT hybrid system, stack stage [18,19]
Seoul National University	Korea	Various part-load control modes for SOFC-only system and SOFC–GT hybrid system [20]
Tsinghua University, University of Science and Technology Beijing	PR China	AspenPlus-based modeling and thermodynamics analysis of SOFC–MGT hybrid system, multi-level simulation platform of SOFC–GT hybrid system based on gPROMS environment [1,2,21]
Shanghai Jiao Tong University	PR China	Dynamic modeling and part-load performance of atmospheric MCFC–GT hybrid system [22]

points), all the polynomial coefficients of β lines can be determined. The β lines are usually selected along the direction of the highest efficiency curve (the polygonal line in Fig. 1). Thus the flow rate, pressure ratio and efficiency can be expressed as nonlinear polynomials of the rational speed and β

$$\phi = \sum_{i=0,j=0}^{n_1} a_{ij}\bar{N}_{cr}^{i}\beta^{j}, \quad \pi = \sum_{i=0,j=0}^{n_2} b_{ij}\bar{N}_{cr}^{i}\beta^{j}, \quad \eta = \sum_{i=0,j=0}^{n_3} c_{ij}\bar{N}_{cr}^{i}\beta^{j} \tag{5}$$

where $\phi = \dot{m}\ (T_{in})^{1/2}/(p_{in}/p_0)$ is the corrected mass flow rate parameter, $N_{cr} = N/(T_{in})^{1/2}$ is the corrected speed parameter, $\bar{N}_{cr} = N_{cr}/N_{cr,0}$ is the dimensionless corrected speed parameter, n_1–n_3 are orders of the polynomials, a_{ij}, b_{ij} and c_{ij} are fitting parameters.

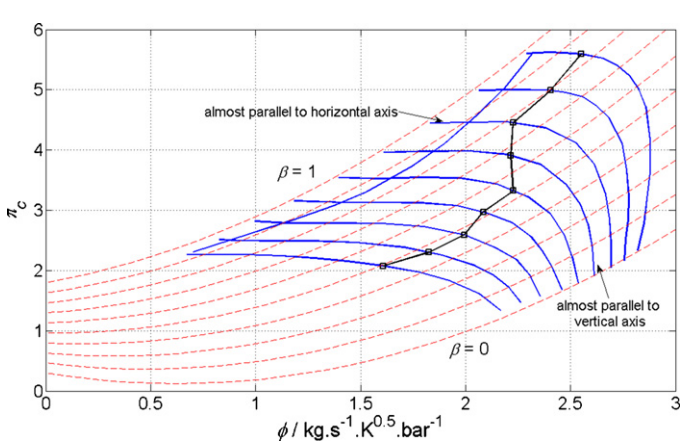

Fig. 1. Typical speed contours of compressor with β line grids.

The turbine can be model similarly using β line grids. However, the turbine inlet chokes above a certain pressure ratio, i.e. the mass flow is no longer a function of the pressure ratio respectively the parameter β. The following elliptic approach instead of a polynomial function is preferred to describe this behavior of constant mass flow rate [12]

$$\phi = a\left[1 - \left(\frac{1-\beta}{b}\right)^{z}\right]^{1/z}, \quad z = c_0 + c_1\bar{N}_{cr} + c_2\bar{N}_{cr}^{2} \tag{6}$$

where a, b and c_0–c_2 are fitting parameters.

2.1.3. Neural network model

Like the above-mentioned J/K model and β line model, turbomachinery modeling is usually based on performance map by fitting the nonlinear relationships between N_{cr}, ϕ, π, and η. In general, two types of functions $\phi = f(\pi, N_{cr})$ and $\pi = f(\phi, N_{cr})$ are both required for system-level analysis, especially for dynamic simulation. From typical speed contours of compressor as shown in Fig. 1, close to the surge zone, the constant speed line is almost parallel to the axis of flow rate. When function in the form $\phi = f(\pi, N_{cr})$ is taken, a small disturbance of pressure ratio leads to a large variation of flow rate, even a multi-value problem appears. Close to the choke zone, function in the form $\pi = f(\phi, N_{cr})$ encounters the similar problem.

Although β line model solves this problem in some extent, it generally requires all the operating data should be within the envelope curve enclosed by the parabolic lines $\beta = 0$ and $\beta = 1$, which means a poor ability of extrapolation. Neural network with a typical

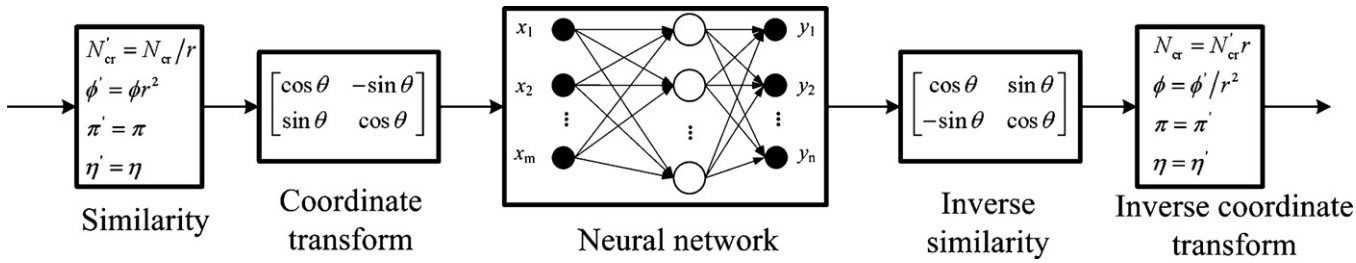

Fig. 2. Flow chart of neural network model of turbomachinery. Whereas, r is the geometric ratio of the actual machine to the original machine (superscript as ′) for similarity, and θ is the rotation angle for coordinate transformation.

topology of feed-forward multilayer perceptron including biases, a sigmoid layer, and a linear output layer is capable of approximating any function with a finite number of discontinuities.

To alleviate the problem of sharp slope in C/T map, the technology of coordinate transform or Givens transform is firstly introduced for map preprocessing [26]. During network training, some preprocessing technologies, such as data normalization and early stopping are used to improve the network generalization. For a general design based on a same original map, the similarity theory is also utilized for the size match [26]. Via training the weights and biases of network, a good interpolation and extrapolation accuracy can be obtained from network output after postprocessing of inverse coordinate transform and inverse similarity. Fig. 2 shows the flow chart of neural network model in our work. For the surge line of centrifugal compressor map, the pressure ratio can be simply expressed as a three-order polynomial of the flow rate.

Considering the effective inertia of shaft, all the above C/T models (except for isentropic efficiency model) can be easily expanded for dynamic analysis.

2.2. Steam methane reformer

Similar to the multi-level SOFC modeling [2], the model library of steam methane reformer also includes quasi-equilibrium, lumped dynamic and distributed dynamic models. Considering the steam reforming reaction ($CH_4 + H_2O \leftrightarrow CO + 3H_2$), water–gas shift reaction ($CO + H_2O \leftrightarrow CO_2 + H_2$) and overall reaction ($CH_4 + H_2O \leftrightarrow CO_2 + 4H_2$) in a fixed bed with Ni-based catalyst, thermodynamic equilibriums are assumed in the quasi-equilibrium model

$$K_{eq,ref} x_{CH_4} x_{H_2O} = \left(\frac{p}{p_0}\right)^2 x_{H_2}^3 x_{CO}, \quad K_{eq,shift} x_{CO} x_{H_2O} = x_{H_2} x_{CO_2} \tag{7}$$

where x_i is the molar fraction of species i, p is the total pressure, K_{eq} is the equilibrium constant.

The standard Langmuir–Hinshelwood expression of reaction kinetics is introduced in lumped and distributed dynamic modeling [27]

$$r_{ref} = \rho_{cat} \frac{k_{ref}}{p_{H_2}^{2.5}} \frac{p_{CH_4} p_{H_2O} - (p_{H_2}^3 p_{CO}/K_{eq,ref})}{(DEN)^2} \tag{8}$$

$$r_{shift} = \rho_{cat} \frac{k_{shift}}{p_{H_2}} \frac{p_{CO} p_{H_2O} - (p_{H_2} p_{CO_2}/K_{eq,shift})}{(DEN)^2} \tag{9}$$

$$r_{overall} = \rho_{cat} \frac{k_{overall}}{p_{H_2}^{3.5}} \frac{p_{CH_4} p_{H_2O}^2 - (p_{H_2}^4 p_{CO_2}/K_{eq,ref} K_{eq,shift})}{(DEN)^2} \tag{10}$$

$$DEN = 1 + K_{CO} p_{CO} + K_{H_2} p_{H_2} + K_{CH_4} p_{CH_4} + \frac{K_{H_2O} p_{H_2O}}{p_{H_2}} \tag{11}$$

where ρ_{cat} is the catalyst density, r_{ref}, r_{shift} and $r_{overall}$ are the reaction rates of reforming, water shift and overall reaction, respectively.

Table 2 lists the kinetic constants $X = k_{ref}$, k_{shift}, $k_{overall}$ or K_i in Eqs. (8)–(11) in Arrhenius-type expression [27]

$$X = A \exp\left(-\frac{E}{RT}\right)\left(\frac{1}{T} - \frac{1}{T_{ref}}\right) \tag{12}$$

For distributed modeling of a tubular packed bed reactor, pressure drop along the axial coordinate can be described by Ergun equation [23], and the convective heat transfer coefficient between gas and solid phase, h_g can be calculated empirically by [28]

$$h_g = 2.03\left(\frac{\rho_g |u_g| \varepsilon_p d_{cat}}{\mu_g}\right)^{0.8} \exp\left(-\frac{3d_{cat}}{r_{in}}\right) \frac{\kappa_g}{2r_{in}} \tag{13}$$

where d_{cat} is the catalyst diameter, r_{in} is the inner radius of tube, ε_p is the void of packed bed, ρ_g, μ_g, κ_g and u_g are the density, dynamic viscosity, heat conductivity and velocity of gas.

By neglecting the dynamics of total gas pressure, $\partial p/\partial t = 0$ and $\partial c_t/\partial t = \partial(p/RT)/\partial t = -(c_t/T)\,\partial T/\partial t$, the total gas mass balance is governed by an ordinary differential equation instead of a partial differential equation [2]. Although this treatment brings stronger numeric couple between mass balance and energy balance of gas phase, it is more reasonable than the assumption of constant gas velocity in some literatures [12,23].

2.3. Heat exchanger

The ε-NTU method is the most general for thermodynamic modeling of heat exchangers. Some analytical relationships between the effectiveness (ε) and number of heat transfer units (NTU) of heat exchanger in different flow modes [29] are collected in our work.

For counter flow which is most commonly used in tube–shell heat exchangers, the ε-NTU function is

$$\varepsilon = \frac{1 - \exp[-NTU(1 - (C_{min}/C_{max}))]}{1 - (C_{min}/C_{max}) \exp[-NTU(1 - (C_{min}/C_{max}))]} \tag{14}$$

where C_{min} and C_{max} means the minimum or maximum heat capacity rate of hot or cold fluids. When $C_{min} = C_{max}$, $\varepsilon = NTU/(1 + NTU)$.

Table 2
Kinetic parameters in Eqs. (8)–(11) by Arrhenius-type expression.

X	A	E (kJ mol^{-1})	T_{ref} (K)
k_{ref} (kmol bar$^{0.5}$ kg$_{cat}^{-1}$ h^{-1})	1.842×10^{-4}	240.1	648
k_{shift} (kmol bar^{-1} kg$_{cat}^{-1}$ h^{-1})	7.558	67.13	648
$k_{overall}$ (kmol bar$^{0.5}$ kg$_{cat}^{-1}$ h^{-1})	2.193×10^{-5}	243.9	648
K_{H_2} (bar^{-1})	0.0296	82.9	648
K_{H_2O}	0.4152	88.68	823
K_{CH_4} (bar^{-1})	0.179	38.28	823
K_{CO} (bar^{-1})	40.91	70.65	648

For cross flow of two unmixed fluids, which is often configured in some compact heat exchangers, such as the recuperator of gas turbines and vehicular radiators, it is

$$\varepsilon = 1 - \exp\left\{\frac{\exp\left[-\mathrm{NTU}(C_{\min}/C_{\max})\mathrm{NTU}^{-0.22}\right] - 1}{\mathrm{NTU}^{-0.22}}\right\} \quad (15)$$

In our previous work, we have presented the quasi-static rating and sizing method of compact heat exchangers in fuel cell systems [30]. We further develop a distributed dynamic model with a set of uniform governing equations for both tube–shell and compact heat exchangers.

As for concurrent or countercurrent flow, along the axial coordinate z, the energy balance of cold (k = c) or hot (k = h) fluid is

$$\rho_k c_{p,k}\frac{\partial T_k}{\partial t} = -\rho_k u_k c_{p,k}\frac{\partial T_k}{\partial z} + \frac{\alpha_k}{\sigma_k}\eta_{o,k}h_k(T_w - T_k) \quad (k = c, h) \quad (16)$$

where ρ, c_p, T, u are the fluid density, mass specific heat, temperature and velocity, T_w is the wall temperature, h is the convective heat transfer coefficient, α is the total heat transfer area per volume of heat exchanger, σ is the ratio of free flow area (A_{free}) to frontal area (A_{fr}) at given fluid side, η_o is the overall surface temperature efficiency.

For gaseous fluid, using the ideal gas law ($\rho = pM/RT$) and neglecting the pressure dynamics ($\partial p/\partial t = 0$), the mass balance of given fluid is governed by

$$0 = -\frac{\partial(\rho_k u_k T_k)}{\partial z} + \frac{1}{c_{p,k}}\frac{\alpha_k}{\sigma_k}\eta_{o,k}h_k(T_w - T_k) \quad (17)$$

The first item can be further reduced to $\partial(\rho u T)/\partial z = (pM/R)\partial u/\partial z$ under assumption of constant pressure. For incompressible fluid, the above equation is replaced by a uniform velocity distribution, $\partial u/\partial z = 0$.

The energy balance of wall is governed by

$$\rho_w c_{p,w}\frac{dT_w}{dt} = \kappa_w\frac{\partial^2 T_w}{\partial z^2} + \frac{1}{A_w}\sum_{k=c,h}A_{\mathrm{free},k}\frac{\alpha_k}{\sigma_k}\eta_{o,k}h_k(T_k - T_w) \quad (18)$$

where κ_w is the heat conductivity of wall, A_w is the section area of wall. In general, the adiabatic boundaries are assumed.

Without considering effects of fins,

$$\eta_{o,k} = 1, \quad \frac{\alpha_k}{\sigma_k} = \frac{1}{r_{\mathrm{hyd},k}} \quad (19)$$

where r_{hyd} is the hydraulic radius at given fluid side, Eqs. (16)–(18) will reduce to the governing equations for tube–shell heat exchangers.

2.4. Ejector

For a gas ejector, the key geometries are the minimum section area of nozzle and the section area of mixing chamber, and the representative thermodynamic parameters include the mass flow rate, pressure and temperature of working flow, induced flow and compressed flow [31]. Governed by mass, momentum and energy balance, the quasi-static gas ejector model for anode recirculation in fuel cell systems has been presented in our previous work [32]. In addition, three critical conditions are also considered here, i.e. the induced flow velocity reaches the critical adiabatic velocity (or local sound velocity) at the inlet or an intermediate section of mixing chamber, or the compressed flow velocity reaches the local sound velocity at the mixing chamber outlet. For gas recirculation in fuel cell systems, the gas ejector model can be further simplified by considering the induced flow and compressed flow as incompressible fluids due to small pressure difference between them [31].

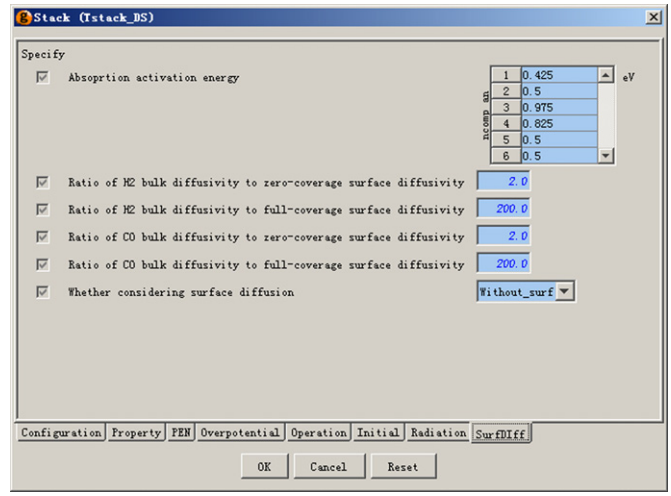

Fig. 3. Graphic specification of distributed SOFC model on the tag of 'surface diffusion'.

2.5. Others

The thermodynamic models or continuous stirred-tank reactor (CSTR) models of other balancing units, such as burner, splitter, mixer, shaft, pipeline and power load, are also included in our SOFC–GT simulation platform. All the unit models in each level are configured with a graphic specification in gPROMS environment. Fig. 3 shows an example of configuration for distributed SOFC model on the Tag of 'surface diffusion'. In additional to the built-in stream interfaces (PMLMaterial and PMLControl) in gPROMS, some special interfaces (radiation interface, power load interface) are also defined for high-level configurations. Thus, users can deploy their simulation flexibly for modular design and analysis.

3. Model validation

The multi-level unit model libraries are validated here by the experimental performance of Siemens–Westinghouse Power Corporation (SWPC) 220 kW pressurized tubular SOFC–GT demonstration hybrid system [33]. The desulfurized fuel (natural gas) is fed into the stack to be reformed and react electrochemically with the preheated air. The cathode outlet gas and the unrecycled anode outlet gas continue to burn in the post-combustion zone of TSOFC. The combustion exhaust firstly preheats the compressed air via the air supply tube (AST), then goes out of stacks and drives a high-pressure (HP) turbine to compress air and sequentially drives a low-pressure (LP) turbine to generate power. The internal reforming inside SOFC stacks includes an indirect internal reforming (IIR) process in an external reformer and a direct internal reforming (DIR) process in the SOFC anode. Anode recirculation via two ejectors is used to provide steam in the external reformer, where the overall strongly endothermic reaction is supported by the radiation energy from SOFC stacks. Some bypass valves are deployed for temperature modulations. Fig. 4 shows the gPROMS realization of the system configuration.

Table 3 lists the characteristics of unit models in Fig. 4. For a simple simulation of full-load and stationery operation, most of unit models are quasi-static in thermodynamics. However, a CSTR model for the external reformer and a distributed dynamic SOFC model with the detailed radiation model are used for better prediction [2,34]. Because of lacking of the C/T performance map, the isentropic efficiency model is applied in this section for all the turbomachineries, and ε-NTU model is used for the recuperator due to

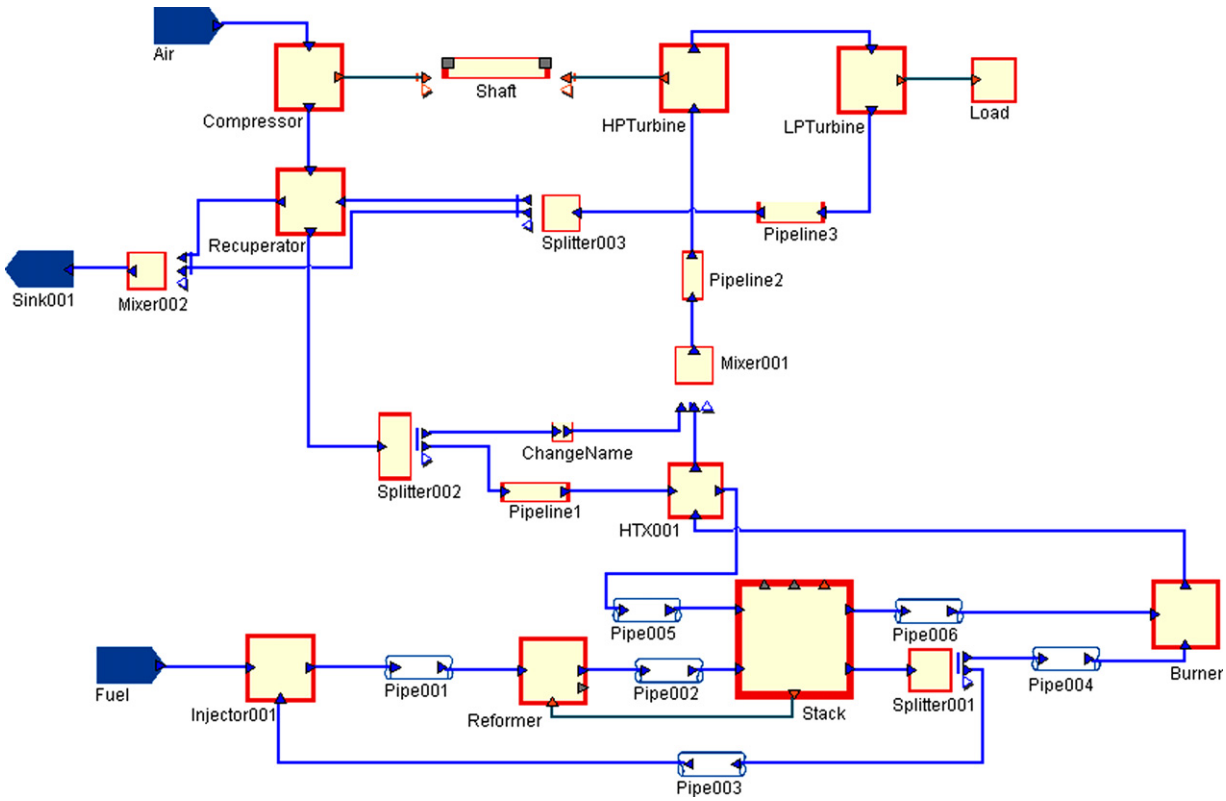

Fig. 4. gPROMS realization of the configuration of SWPC SOFC–GT demonstration system.

the same reason. Pipeline1–3 are configured to describe the system heat loss.

Table 4 shows the structural parameters and physical properties of SOFC. The interface-type positive–electrolyte–negative (PEN) transport model is used by considering the small anode thickness, the ohmic polarization is calculated by transmission-line model, and the activation polarization is obtained by Arrhenius-type expressions of activation resistance. Table 5 shows some parameters related to electrochemical kinetics [35] and Table 6 shows the parameters related to flow and heat transfer [12,36].

Tables 7 and 8 compare the system performance and status parameters of stream temperature (°C), pressure (bar) and mass flow rate (kg s^{-1}) in the base case among the experimental data, simulation results of advanced power system analysis tool (APSAT)

Table 3
Name and property of unit models in Fig. 4.

Unit model name	Model function and property
Fuel	'Source' model in gPROMS for inlet natural gas
Air	'Source' model in gPROMS for inlet air
Sink001	'Sink' model in gPROMS for atmosphere
Stack	Distributed dynamic model for tubular SOFC stack
Compressor	Isentropic efficiency model for compressor
HPTurbine	Isentropic efficiency model for high-pressure turbine
LPTurbine	Isentropic efficiency model for low-pressure turbine
Reformer	Lumped dynamic model for DIR reformer
Recuperator	ε-NTU thermodynamic model for recuperator
HTX001	ε-NTU model for air supply tube (AST) in TSOFC
Injector001	Gas ejector model for two anode ejectors
Burner	Quasi-static model for post-combustion zone in TSOFC
Load	Power load model for generator
Splitter001–003	Splitter model for bypass
Mixer001–002	Mixer model for stream mixer
Shaft	Power balance model for C/T shaft
Pipe001–006	Linear flow resistance model
Pipeline1–3	Linear flow resistance model with heat loss

Table 4
Structural parameters and physical properties of TSOFC.

Description	Value
Anode thickness (m)	1.0×10^{-4}
Cathode thickness (m)	2.2×10^{-3}
Electrolyte layer thickness (m)	4.0×10^{-5}
Anode porosity	0.4
Anode tortuosity	3
Cathode porosity	0.5
Cathode tortuosity	1.5
Electrolyte conductivity (S m^{-1})	$3.34 \times 10^4 \cdot \exp(-10300/T)$
Anode electronic conductivity (S m^{-1})	$9.5 \times 10^7/T \cdot \exp(-1150/T)$
Cathode electronic conductivity (S m^{-1})	$4.2 \times 10^7/T \cdot \exp(-1200/T)$
Interconnector conductivity (S m^{-1})	$9.3 \times 10^6/T \cdot \exp(-1100/T)$
Cell tube outer radius (m)	1.1×10^{-2}
Cell length (m)	1.5
AST inner radius (m)	2.5×10^{-3}
AST outer radius (m)	4×10^{-3}
Gap between cell tubes (m)	2×10^{-3}
Interconnector perimeter (m)	6×10^{-3}
Interconnector thickness (m)	1×10^{-3}
Serial cell number	384
Parallel cell number	3
Anode density (kg m^{-3})	7740
Anode mass specific heat (J kg^{-1} K^{-1})	300
Cathode density (kg m^{-3})	7740
Cathode mass specific heat (J kg^{-1} K^{-1})	300
Anode density (kg m^{-3})	5300
Anode mass specific heat (J kg^{-1} K^{-1})	400
Electrolyte density (kg m^{-3})	6000
Electrolyte mass specific heat (J kg^{-1} K^{-1})	500
AST density (kg m^{-3})	3970
AST mass specific heat (J kg^{-1} K^{-1})	1167
Anode thermal conductivity (W m^{-1} K^{-1})	6.23
Cathode thermal conductivity (W m^{-1} K^{-1})	9.6
Electrolyte thermal conductivity (W m^{-1} K^{-1})	2.7
Electrolyte thermal conductivity (W m^{-1} K^{-1})	2.7
PEN emissivity	0.8
AST emissivity	0.2

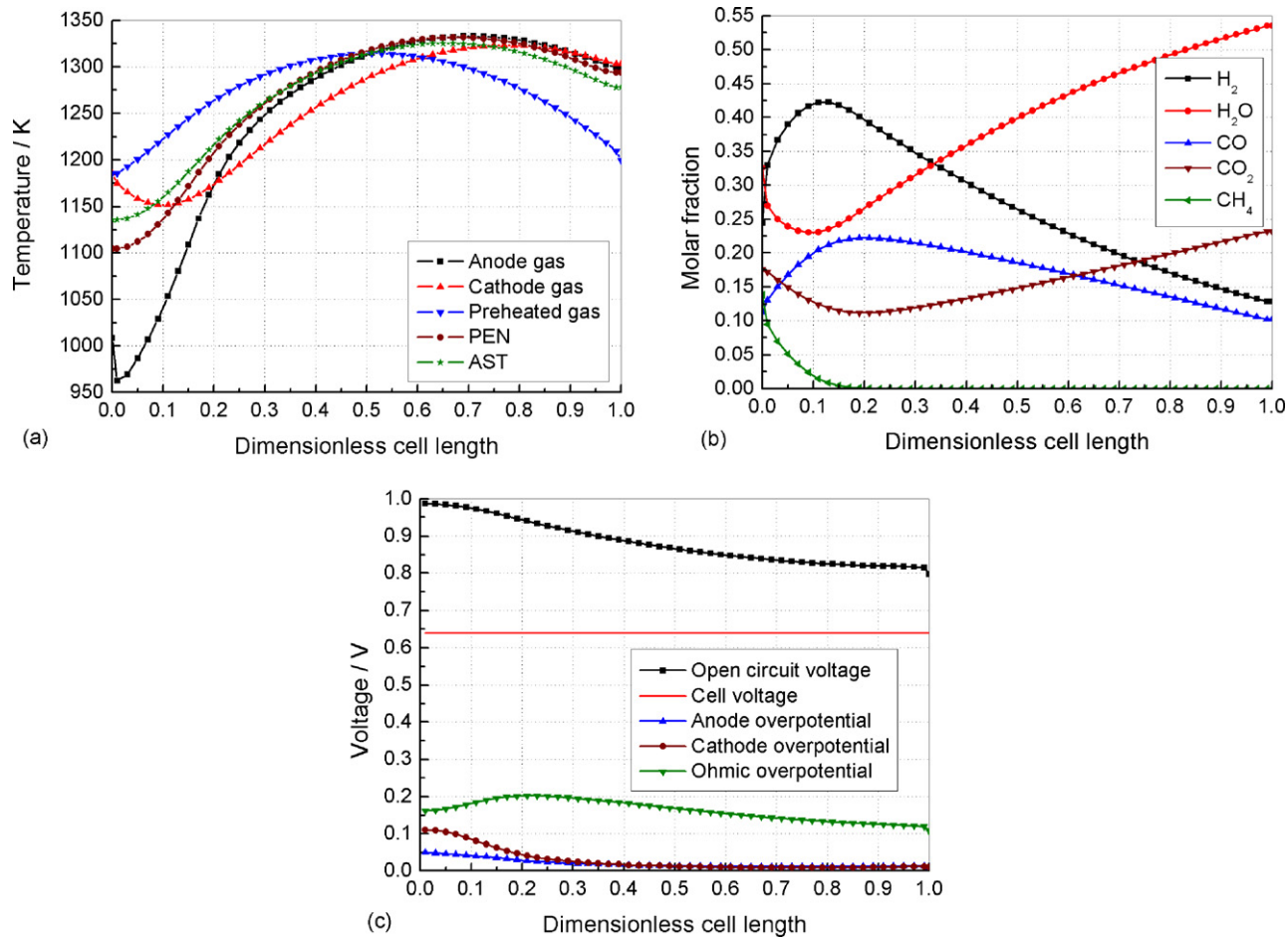

Fig. 5. Axial distribution of (a) temperatures of anode gas, cathode gas, preheated air, PEN and AST, (b) fuel concentrations, and (c) polarizations in SOFC.

[33] and our model. In our calculation, the turbine generation power, SOFC cell voltage and SOFC operating pressure are set as the experimental data. It is considered more reasonable to get the average SOFC temperature from the temperature distribution instead of setting it as APSAT did. Here, the stack operating temperature is the average value among axial distribution of PEN temperature, and the system efficiency is calculated based on the lower heating value of natural gas (49,810 kJ kg^{-1}) [33]. Mainly due to our advanced distributed SOFC model with the detailed radiant model [2], most of our calculation obtained a smaller relative error (less than 1%) than what APSAT did.

More importantly, superior to APSAT, the distributed SOFC model provides the information of local parameters. Fig. 5(a) shows the temperature distributions of the anode gas, cathode gas, preheated air, PEN and AST along the tube length. Because of the strong endothermic reaction of methane reforming, both the gas temperature and solid temperature decrease firstly close to the anode inlet, then increase gradually due to the exothermic electrochemical reaction. The gap between the highest and lowest cell temperature (almost 130 K) means a significant temperature gradient, i.e. the temperature of hot spots is much higher than the average temperature, which supports the necessity of distributed SOFC modeling with reasonable numeric cost. On the other hand, at the anode and cathode outlet where the cell temperature is the highest under co-flow condition, the gas temperatures are almost equal to the local solid temperature due to full convective heat

Table 5
Parameters related to electrochemical kinetics in TSOFC.

Parameter	Symbol	Value
Anode activation energy (J mol^{-1})[a]	E_a	1.1×10^5
Cathode activation energy (J mol^{-1})[a]	E_c	1.6×10^5
Pre-exponent factor of H_2 kinetics (A m^{-2})[a]	k_{H_2}	2.13×10^8
Pre-exponent factor of CO kinetics (A m^{-2})	k_{CO}	5.0×10^7
Pre-exponent factor of O_2 kinetics (A m^{-2})[a]	k_{O_2}	1.49×10^{10}
H_2 and CO reaction order[a]	m	0.25
O_2 reaction order[a]	m	0.25

[a] From Ref. [35].

Table 6
Parameters related to flow and heat transfer in TSOFC.

Parameter	Symbol	Value
Nusselt number for anode gas channel[a]	Nu_a	Zhukauskas correlation
Nusselt number for cathode gas channel[a]	Nu_c	4.4
Nusselt number for inner AST[a]	$Nu_{AST,in}$	Gnilinski correlation
Nusselt number for outer AST[a]	$Nu_{AST,out}$	6.0
Friction factor of anode gas[a]	f_a	80
Friction factor of cathode gas[a]	f_c	90
Friction factor of air in AST[a]	f_{air}	64
Pressure loss coefficient at anode inlet[b]	$\zeta_{a,in}$	0.5
Pressure loss coefficient at anode outlet[b]	$\zeta_{a,out}$	0.5
Pressure loss coefficient at cathode inlet[b]	$\zeta_{c,in}$	0.5
Pressure loss coefficient at cathode outlet[b]	$\zeta_{c,out}$	0.5
Pressure loss coefficient at AST inlet[b]	$\zeta_{AST,in}$	0
Pressure loss coefficient at AST outlet[b]	$\zeta_{AST,out}$	1.0
Radiation heat from SOFC to pre-reformer (kW)	q	20

[a] From Ref. [36].
[b] From Ref. [12].

Table 7
Comparison of system performance among experiments, APSAT and our model.

Performance	Experiments	APSAT	Our model
Turbine generation power (kW)	21	21.6	21
SOFC operating temperature (°C)	995	1000	998.05
SOFC operating pressure (bar)	2.9	2.94	2.9
SOFC cell voltage (V)	0.639	0.633	0.639
SOFC stack voltage (V)	244	243.1	245.376
SOFC stack current (A)	700	694.2	699.65
SOFC stack power (kW)	170.8	168.78	171.677
Total AC power (kW)	183.45	181.94	184.09
System efficiency (%)	52.44	52.0	52.62

transfer. As a result, the gas outlet temperature of SOFC is actually much higher than that from lumped modeling, which is meaningful for the control strategy of TIT.

Fig. 5(b) shows the concentration distributions of fuel components. Close to the anode inlet, concentrations of H_2 and CO increase, while concentrations of methane and H_2O decrease resulting from steam reforming reaction. As the reforming reaction is enhanced due to H_2 consumption by electrochemical reaction, methane is almost fully converted before the middle section of anode flow channel. At the lower part of anode channel where electrochemical reactions dominate, H_2 and CO are reacted and H_2O and CO_2 are produced, while the gas molar concentrations obey the thermodynamic equilibrium of water gas shift reaction. Fig. 5(c) shows the polarizations distribution. As fuel concentration decreases and cell temperature increases, the open circuit voltage appears to decrease. At the low-temperature zone close to the fuel inlet, the activation overpotential is relatively high and the ohmic overpotential possesses almost 50–60% in the total overpotential. As the PEN temperature increases, the ohmic overpotential is more than 70% of the total overpotential. So the ohmic loss is the dominant polarization in tubular SOFCs.

As shown in Fig. 6(a), the local current density shows a non-monotonic distribution under coflow condition. The cell temperature is low at the inlet section of flow channel, while the fuel and oxygen concentration is low at the outlet section of flow channels, which leads to a maximum of local current density at the middle section. Fig. 6(b) shows the fraction of H_2 electrochemical current in the total current density, where more than 80% current density attributes by H_2 electrochemical oxidation due to higher kinetics of H_2 than that of CO. Fig. 6(c) and (d) shows the local gas velocities in the anode and cathode channel, respectively. With a small pressure drop, the increment of gas temperature leads to increasing gas velocity at the anode side, while the gas velocity at the cathode side shows a non-monotonic variation due to trade-off between the decrement of gas concentration and the increment of gas temperature.

The neural network model of turbomachinery in Section 2.1.3 is validated separately based on the performance maps of C/T from Ref. [37], which has been used in some literatures [12,17]. As shown in Fig. 7, the neural network model with preprocessing of coordinate transfer has the ability to obtain a good interpolation and extrapolation accuracy.

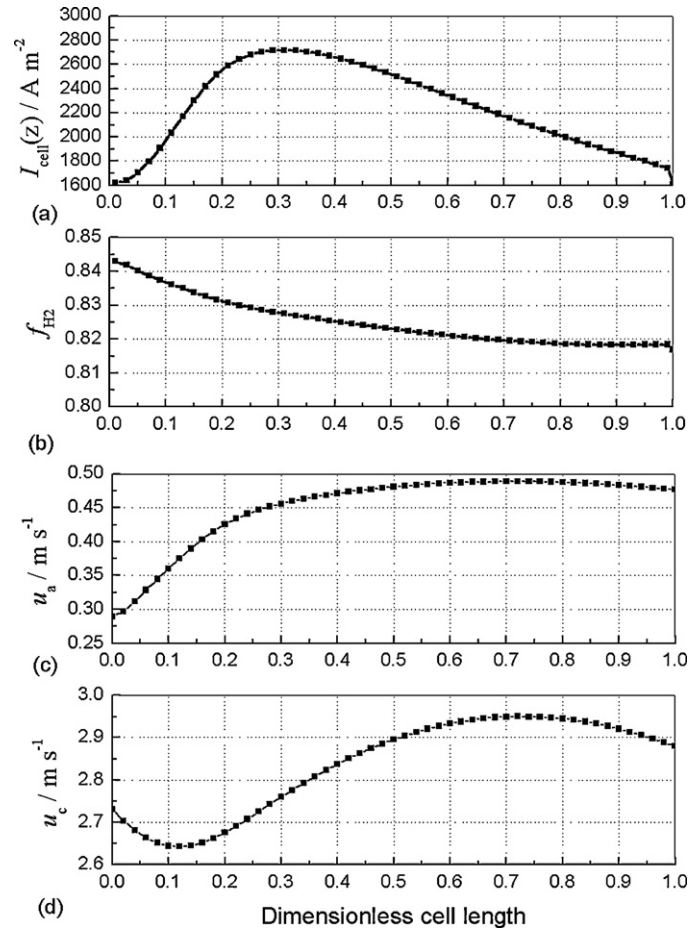

Fig. 6. Axial distribution of (a) local current density, (b) fraction of H_2 electrochemical current in the total current density, (c) anode gas velocity, and (d) cathode gas velocity in SOFC.

4. Reverse design of units and system dynamics analysis

During the part-load or dynamic operation, performance of units generally deviates from that at design point, especially for some fast-response units (e.g. gas ejector). Due to lacking of open data, reverse sizing is necessary for this rating problem. In this section, based on the full-load and stationery data, the recuperator and ejector are designed reversely for analysis of part-load and dynamic performance.

Table 8
Comparison of system status among experiments, APSAT and our model.

Status (T, p, $\dot{m}$)	Experiments	APSAT	Our model
Compressor inlet	15, 1.013, 0.635	15, 1.01, 0.635	15, 1.013, 0.635
Compressor outlet	155, 3, 0.635	147, 3, 0.635	147.2, 3, 0.635
Recuperator cool-side outlet	500, 2.9, 0.635	500, 2.94, 0.635	500.2, 2.9, 0.635
SOFC inlet air bypass	500, 2.9, 0.14	500, 2.94, 0.14	500.2, 2.9, 0.14
SOFC inlet air (after pipe1)	500, 2.9, 0.495	497, 2.94, 0.495	500.2, 2.9, 0.495
SOFC exhaust (after burner)	780, 2.8, 0.502	770, 2.82, 0.502	783.06, 2.83, 0.502
HP turbine inlet (before pipe2)	730, 2.8, 0.642	714, 2.82, 0.642	724.7, 2.8, 0.642
HP turbine outlet	610, –, 0.642	575, 1.54, 0.642	579.8, 1.374, 0.642
LP turbine outlet (before pipe3)	550, –, 0.642	545, 1.24, 0.642	551.3, 1.194, 0.642
System exhaust	210, 1.1, 0.642	202, 1.22, 0.642	206.8, 1.1, 0.642
SOFC fuel inlet	15, –, 0.007	15, 2.94, 0.007	15, 2.9, 0.007

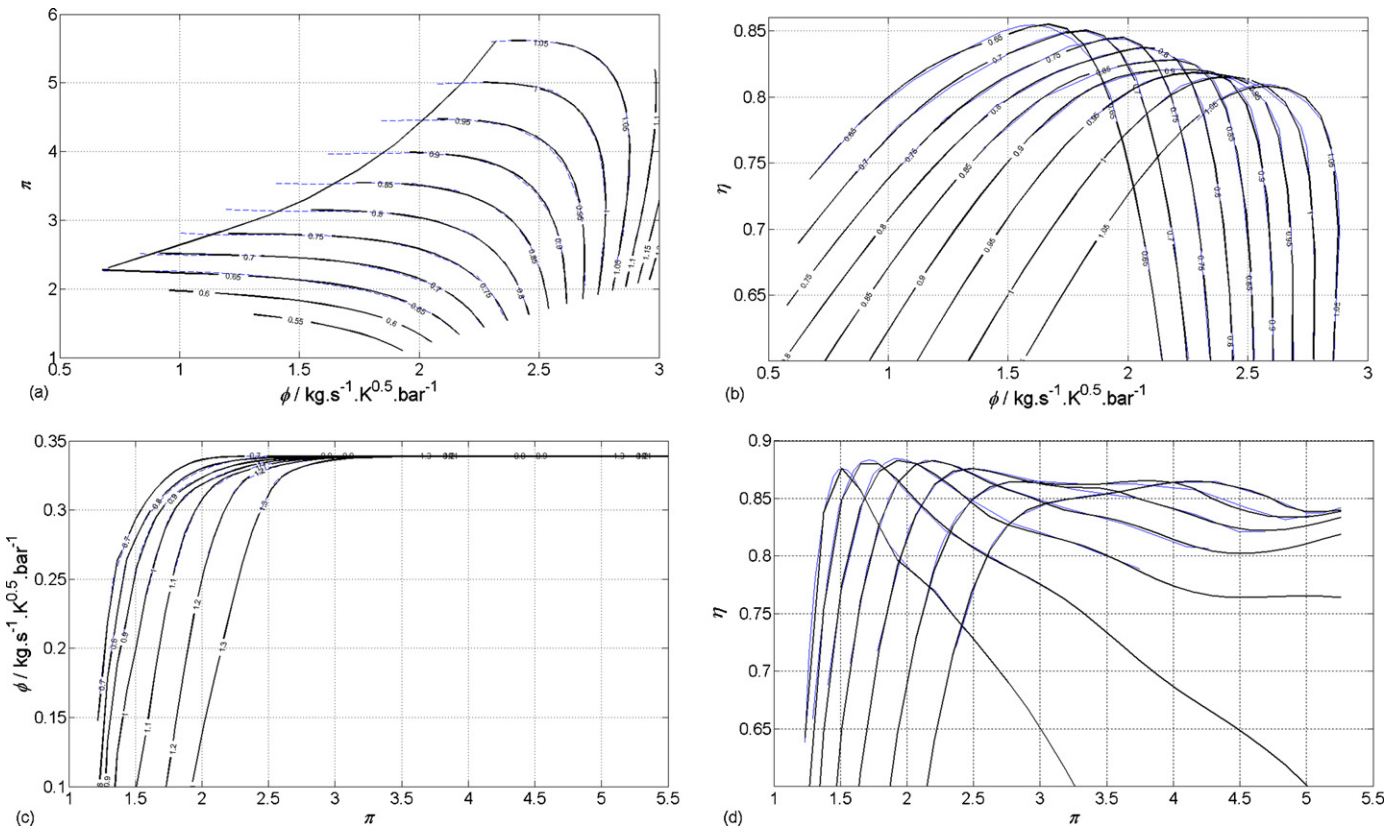

Fig. 7. Neural network model of turbomachinery: (a) and (b) are dimensionless speed contours of compressor, (c) and (d) are dimensionless speed contours of HP turbine. Dashed lines are original and solid lines are from network outputs.

4.1. Reverse design of units

The recuperator here is a cross-flow, plate-fin compact heat exchanger, where 3/8-6.06 blind-type surface is chosen at the air side and 11.11 surface is used at the side of high-temperature exhaust [29]. Table 9 lists the design parameters of recuperator and two ejectors from their full-load operating data.

As a result, the recuperator size is: length of air-side flow path is 5.06 m, length of high temperature exhaust flow path is 4.04 m, and non-fluid path length is 0.07 m, which means cold-side and hot-side frontal areas of 0.317 and 0.316 m^2, respectively and volume of recuperator of 1.6 m^3. Note that for a highly efficient gas–gas compact heat exchanger, due to nearly equal heat capacity rate of hot or cold fluids in this application ($C_{min}/C_{max} \approx 1$), the target effectiveness and target pressure drop has a significant impact on the recuperator size. For example, when the target effectiveness is given as $\varepsilon = 0.85$, the dimensions of recuperator is $2.74 \times 2.85 \times 0.08$ m, which is much smaller than that when $\varepsilon = 0.89$ in Table 9.

With the design parameter of ejectors in Table 9, the minimum diameter and outlet diameter of nozzle are 2.06 and 2.07 mm, respectively, and the diameter of mixing chamber is 5.89 cm.

Table 9
Design parameters of recuperator and ejectors.

Parameter	Value
Recuperator	
Effectiveness	0.89
Cold-side target relative pressure drop (%)	0.5
Hot-side target relative pressure drop (%)	2
Air flow rate (kg s^{-1})	0.635
Inlet air pressure (bar)	1.01325
Inlet air temperature (K)	419.5
Exhaust gas flow rate (kg s^{-1})	0.615
Inlet exhaust gas pressure (bar)	1.2
Inlet exhaust gas temperature (K)	817
Exhaust composition (H_2O–CO_2–O_2–N_2)	3.76% H_2O–1.89% CO_2–16.85% O_2–77.5% N_2
Ejector	
Mass flow rate of working fluid (kg s^{-1})	0.0035
Working fluid temperature (K)	288.15
Working fluid pressure (bar)	6
Mass flow rate of induced fluid (kg s^{-1})	0.0186
Induced fluid temperature (K)	1300
Induced fluid pressure (bar)	2.89
Induced fluid composition	12.9% H_2–53.5% H_2O–10.2% CO–23.2% CO_2–0.2% N_2
Compressed fluid pressure (bar)	2.905

4.2. Part-load and dynamic operating

In our multi-level model library, most of unit models can be used for dynamic analysis. Fig. 8 shows a dynamic process corresponding to the load variation. As shown in Fig. 8(a), due to ohmic loss, the cell current decreases immediately as the cell voltage increases, then gradually goes to a new steady state. The tendency of first decrement and then increment of the stack current shows characteristics of non-minimum phase. Fig. 8(b) shows the variation of fuel concentrations at the anode outlet. As the stack current decreases, the concentration of H_2, CO and O_2 increase and the concentration of H_2O and CO_2 decrease. Due to the buffering effect of volume of gas flow channel, the fuel concentration varies smoothly without a sudden change like the cell voltage–current relationship. Fig. 8(c) shows the transient injection coefficient of ejectors, which is defined as the ratio of induced fluid flow rate to working fluid flow rate.

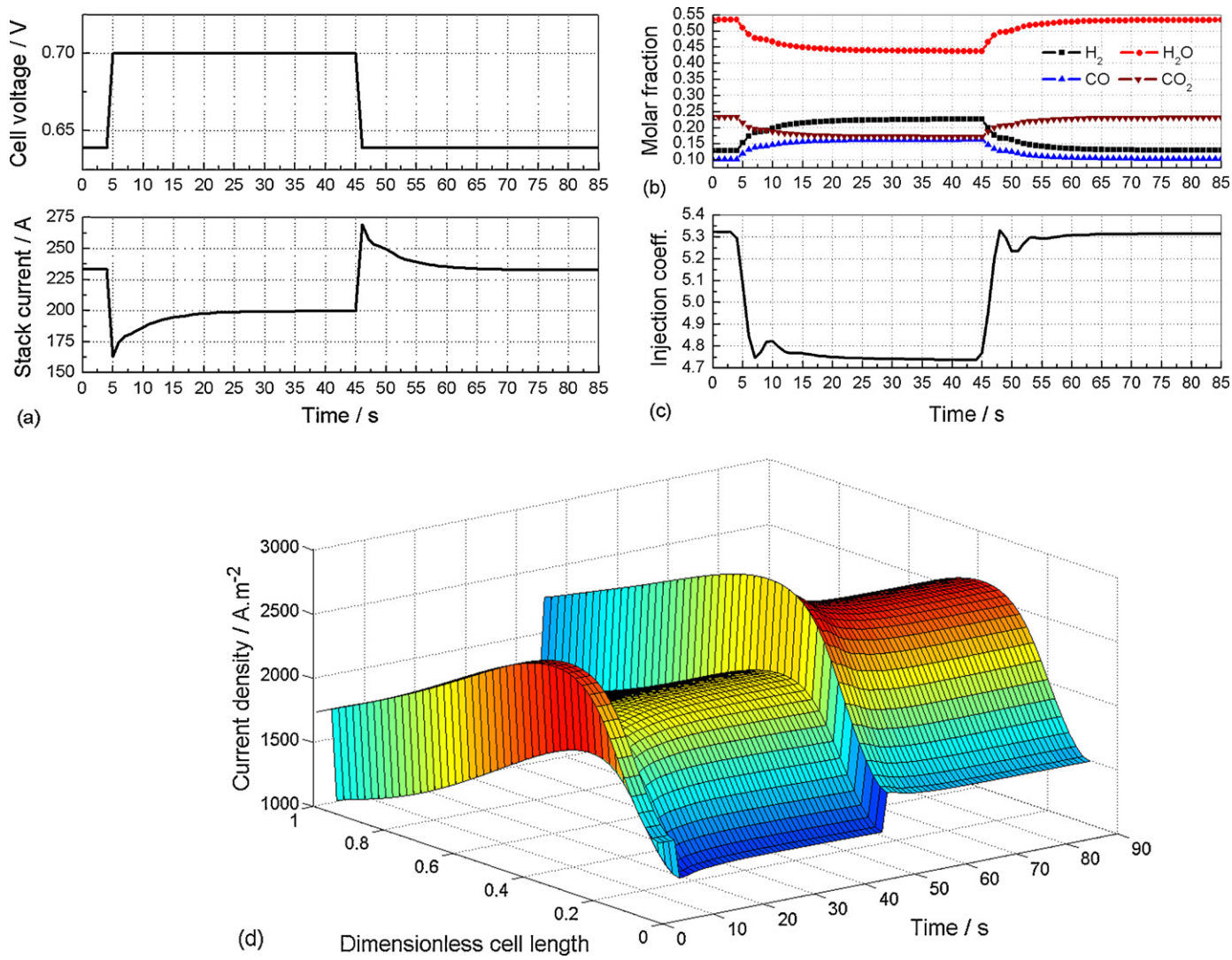

Fig. 8. Dynamics of (a) cell voltage and stack current, (b) anode outlet fuel concentration, (c) injection coefficient of ejectors, and (d) temporal variation and spatial distribution of local current density during a variable SOFC load.

From this part-load and dynamic process, we can find the time constant of SOFC stack in SWPC demonstration system is almost 15 s, which is dominant by gas filling dynamics in the flow channel. As shown in Fig. 6(c), the average velocity of anode gas is almost 0.45 m s^{-1}, for the cell length of 1.5 m, the corresponding gas residence time of 3.3 s is almost one fifth of the stack time constant. Fig. 8(d) shows the temporal variation and spatial distribution of local current density. Note that the solid temperatures do not reach the steady state during the total transient process.

5. Conclusion

This paper presented the model libraries of turbomachinery, steam methane reformer, heat exchanger, ejector and other balancing units. The characteristics of our SOFC–GT simulation platform are summarized as follows:

(1) Compared to APSAT and other state-of-the-art SOFC–GT simulation tool, the biggest advantage is the integrated hierarchical modeling framework of natural gas IRSOFC, which has been presented in details in Ref. [2]. And the equation-based solver of gPROMS is very suitable for distributed SOFC modeling.
(2) The multi-level models of balancing units include part of state-of-the-art achievements and also our specific work of, e.g. neural network model with coordinate transform processing of turbomachinery, uniform distributed modeling of tube–shell and compact heat exchangers, etc.
(3) The distributed modeling is available to reasonable prediction of the hot spot and the outlet gas temperature for high-temperature application, which is significant for the safe operation of SOFC and control strategy of TIT.
(4) Validated by the steady-state experimental data of SWPC demonstration SOFC–GT hybrid system, our prediction for system performance and system status shows more accurate than that from APSAT [33].
(5) Most of unit models can be used for both rating and sizing problem, and provide transient mechanism part-load and dynamic analysis.
(6) With graphic specification of each unit model, our multi-level SOFC–GT simulation platform is available for flexible configuration and modular design like commercial process simulation software do.

All these work provide a good fundament for system design, optimization and control algorithms in the future.

Acknowledgement

Financial support from the Natural Science Foundation (Project No. 50706019) is gratefully acknowledged.

References

[1] C. Bao, Y.X. Shi, C. Li, N.S. Cai, Q.Q. Su, Int. J. Hydrogen Energy 35 (2010) 2894–2899.
[2] C. Bao, Y.X. Shi, E. Croiset, C. Li, N.S. Cai, J. Power Sources 195 (2010) 4871–4892.
[3] A.D. Rao, A thermodynamic analysis of tubular SOFC based hybrid systems: [DS Dissertation], University of California, Irvine, 2001.
[4] R.A. Roberts, A dynamic fuel cell–gas turbine hybrid simulation methodology to establish control strategies and an improved balance of plant: [DS Dissertation], University of California, Irvine, 2005.
[5] E.A. Liese, R.S. Gemmen, J. Eng. Gas Turb. Power 127 (2005) 86–90.
[6] R.J. Braun, Optimal design and operation of solid oxide fuel cell systems for small-scale stationary applications: [DS Dissertation], University of Wisconsin, Madison, 2002.
[7] M.D. Lukas, K.Y. Lee, H. Ghezel-Ayagh, Control Eng. Pract. 10 (2002) 197–206.
[8] P. Costamagna, L. Magistri, A.F. Massardo, J. Power Sources 96 (2001) 352–368.
[9] L. Magistri, L.A. Traverso, F. Cerutti, M. Bozzolo, P. Costamagna, A.F. Massardo, Fuel Cells 5 (2005) 80–96.
[10] P. Lunghi, S. Ubertini, J. Eng. Gas Turb. Power 124 (2002) 858–866.
[11] E. Riensche, U. Stimming, G. Unverzagt, J. Power Sources 171 (1998) 251–256.
[12] C. Stiller, Design, operation and control modelling of SOFC–GT hybrid systems: [DS Dissertation], Norwegian University of Science and Technology, Trondheim, 2006.
[13] J. Palsson, A. Selimovic, L. Sjunnesson, J. Power Sources 86 (2000) 442–448.
[14] A. Selimovic, J. Palsson, J. Power Sources 106 (2002) 76–82.
[15] S.F. Au, S.J. McPhail, N. Woudstra, K. Hemmes, J. Power Sources 122 (2003) 37–46.
[16] W. Zhang, E. Croiset, P.L. Douglas, M.W. Fowler, E. Entchev, Energy Convers. Manage. 46 (2005) 181–196.
[17] S.H. Chan, H.K. Ho, Y. Tian, J. Power Sources 114 (2003) 213–227.
[18] H. Uechi, S. Kimijima, N. Kasagi, J. Eng. Gas Turb. Power 126 (2004) 755–762.
[19] M. Yokoo, T. Take, S. Ohtsu, Electr. Eng. Jpn. 147 (2004) 11–19.
[20] J.S. Yang, J.L. Sohn, S.T. Ro, J. Power Sources 166 (2007) 155–164.
[21] Y.X. Shi, N.S. Cai, Z.S. Li, J. Tsinghua Univ. 45 (2005) 1142–1146 (Science and Technology, in Chinese).
[22] H.S. Zhang, S.L. Weng, M. Su, J. Fuel Cell Sci. Technol. 2 (2005) 94–98.
[23] Process Systems Enterprise Ltd., gPROMS Process Model Library (PML), London, 2004.
[24] P. Moraal, I. Kolmanovsky, Turbocharger Modeling for Automotive Control Applications, SAE paper 1999-01-0908 (1999).
[25] J. Kurzke, Preparing compressor maps for gas turbine performance modeling, 2009, http://www.gasturb.de/Free/Manuals/SmoothC82Manual.pdf.
[26] C. Bao, M.G. Ouyang, B.L. Yi, J. Power Sources 156 (2006) 232–243.
[27] J. Xu, G.F. Forment, AIChE J. 35 (1989) 88–96.
[28] C.H. Li, B.A. Finlayson, Chem. Eng. Sci. 32 (1977) 1055–1066.
[29] W.M. Kays, A.L. London, Compact heat exchangers, third ed., McGraw-Hill, New York, 1984.
[30] C. Bao, M.G. Ouyang, B.L. Yi, Int. J. Hydrogen Energy 31 (2006) 1040–1057.
[31] E.R. Sokolow, H.M. Zinger, Injector, Science Publishing Company, 1977 [in Chinese].
[32] C. Bao, M.G. Ouyang, B.L. Yi, Int. J. Hydrogen Energy 31 (2006) 1879–1896.
[33] Y.F. Yi, T.P. Smith, J. Brouwer, A. Rao, S. Samuelsen, Simulation of a 220 kW hybrid SOFC gas turbine system and data comparison, Electrochemical Society Proceedings on SOFC VIII, Paris, 2003, pp. 1442–1454.
[34] C. Bao, N.S. Cai, E. Croiset, J. Power Sources 196 (2011) 3223–3232.
[35] E. Achenbach, J. Power Sources 49 (1994) 333–348.
[36] W.M. Rohsenow, J.P. Hartnett, Y.I. Cho, Handbook of Heat Transfer, third ed., McGraw-Hill, 1998.
[37] J. Kurzke, Compressor and Turbine Maps for Gas Turbine Performance Computer Programs – Component Map Collection 2, Dachau, Germany, 2004.